

Modeling and Control of a Tailsitter UAV

Romain Chiappinelli¹ and Meyer Nahon²

Abstract—Unconventional UAVs are being proposed to combine the benefits of fixed-wing and rotary-wing aircraft. Among these are tailsitter aircraft, which are fixed-wing aircraft with vertical landing capability. In this work, we present the development of a real-time simulation of a commercial radio-controlled tailsitter aircraft, along with a single controller that is capable of executing vertical takeoff, level flight, and vertical landing. The model accounts for progressive stall, the effect of large control surface deflections, as well as the drag generated by the aircraft's structural components. The thruster model accounts for changes in battery voltage, inflow velocity, and predicts slipstream effects. A ground contact model is also implemented to allow simulation of the takeoff and landing phases. A cascaded quaternion-based controller is then implemented in this simulated environment to control the tailsitter in a typical flight mission, with promising results. The transition from level flight to hover proves to be the most challenging aspect in the control of this aircraft.

I. INTRODUCTION

Unmanned aerial vehicles (UAVs) are used or proposed in many civilian and military applications such as search and rescue, monitoring, agriculture management, aerial photography, and 3D mapping [1]. UAVs are usually classified into two categories: rotor-craft, which are preferred for their maneuverability and hover capability, while lacking flight efficiency; and fixed-wing aircraft, which possess better flight efficiency but usually lack maneuverability. Between these two categories lies the Vertical Take-Off and Landing (VTOL) fixed-wing aircraft, sometimes called hybrid aircraft [2], able to perform both hovering and efficient flight. In this category, a flying wing tailsitter is chosen here as a case study of the modeling and control challenges associated with these unconventional aircraft. This platform is a fixed wing aircraft that is able to perform vertical maneuvers with the nose and thrusters pointing upward. Its high thrust to weight ratio and large control surfaces with large deflections allow vertical takeoff, hovering, and vertical landing. In order to achieve the transition from hovering flight, the entire aircraft must pitch down to enter high efficiency level flight.

Aerodynamic forces and moments are usually assumed to vary with the airflow velocity squared, allowing the use of aerodynamic coefficients that vary only with the angle of attack (AOA). To cover the full flight envelope, aerodynamic coefficients are sometimes modeled as second order sine and cosine functions of the angle of attack, such as in [3].

¹Romain Chiappinelli is a Master Student in the Department of Mechanical Engineering, McGill University, Montreal, QC, Canada
romain.chiappinelli@mail.mcgill.ca

²Meyer Nahon is a Professor in the Department of Mechanical Engineering, McGill University, Montreal, QC, Canada
meyer.nahon@mcgill.ca

However, aerodynamic stall is not represented in this model. In [4], third order trigonometric functions are used to capture the effects of stall. These functions behave similarly to flat plate models [5]. Stall effects can also be modeled as a sigmoid function to blend the linear range with the flat plate model for high AOA [6], as it is known that once stalled, the profile of an airfoil has negligible effect on its aerodynamic performance [7]. The effects of control surface deflections are often modeled linearly, such as in [3]. A more empirical method was used in [8], where the force and moment model was implemented as a quadratic curve fit of the velocity, angle of attack, motor rpm and elevon deflection data, based on wind tunnel experiments of half the aircraft.

A very relevant simulator, reported by Selig [9], was developed to model small scale aerobatic fixed-wing aircraft. It uses a component breakdown approach, where the wing is split into several segments, each producing a lift force, drag force, and pitching moment. The aerodynamic coefficients for these three quantities are precomputed for the full angle of attack range and control surface deflection, and are retrieved during simulation by linear interpolation.

In this research, the component breakdown approach used for the aerodynamic simulation is based on the work by Khan [10]. Flat-plate theory is used to compute the aerodynamic coefficients in real-time for each segment of the wing based on the inflow velocity and control surface deflection. In the present work, we add additional effects, such as ground contact and parasitic drag of the landing gear and other appendages. In addition, the thrusters are modeled using bench test data and a propeller database. The propeller slipstream is considered using momentum theory.

The aircraft studied here is a commercial radio controlled platform: the X-VERT VTOL from Horizon Hobby shown in Fig. 1. This flying wing platform weighs about 0.2 [kg] and has a wing span of about half a meter. It is equipped with two thrusters, creating slipstream over two control surfaces called elevons (elevator+ailerons). In combination, the four actuators can generate roll, pitch, and yaw moments, while a longitudinal force is achieved through common thrust.

Several successful control strategies were reported by the research community. The very different aerodynamics associated with large attitude changes make the control task challenging. To overcome this difficulty, controllers based on the flight mode were derived, such as switching logic choosing between hover and level flight linear controller [11], gain scheduling with an adaptive method for attitude control [12], or a hybrid controller [13], which uses different dynamic models for hover, transition, and level flight, with a separate controller for each. Other types of adaptive

based controllers were developed, such as in [14], which uses recursive least squares to estimate a linear function relating deflections to angular acceleration. Backstepping is then applied on this accurate dynamic model to control the attitude. More recently, an adaptive method was used to estimate the aerodynamics from basis functions, and a cascaded architecture controller was used to track a path [4]. Precomputed optimal body rates as a function of the attitude error were used for the attitude controller.

In this work, the controller developed is a single quaternion-based controller, originally developed for aerobatic aircraft. It does not assume any particular operating condition and is able to perform well through large attitude changes [15]. Its cascaded architecture is adaptable to many platforms with minimal modifications, allowing it to be used for the tailsitter in this research. The controller is shown in simulation to successfully accomplish a typical flight mission that includes vertical takeoff, transition, level flight, descent, and vertical landing.

II. AIRCRAFT SIMULATION

The real-time simulator is implemented in Simulink using the *Real-Time Sync* block running at 200 [Hz]. The model considers the aircraft as made up of several components, each creating forces and moments, which are then translated to the center of mass (CM) and finally fed to the equations of motion. The wing aerodynamics are based on a flat-plate model, using the work of Khan [10]. His component breakdown model considers the full flight envelope aerodynamics, stalling effects, partial flow conditions over the wing surfaces, low aspect ratio, and large control surfaces with large deflections.

Other components modeled in the simulator include the propeller protectors and landing gear, which are approximated as rod segments that result in pure drag forces. The left and right thrusters, which are assumed in the same plane as the center of mass, generate the left and right thrust forces T_l and T_r along the longitudinal axis, and left and right torques Q_l and Q_r . In addition, gyroscopic moments are modeled using the left and right propeller rotational speeds ω_l and ω_r . To simulate takeoff and landing phases, ground contact forces are generated when the aircraft touches the ground. Finally, the simulator implements a Dryden wind turbulence model [16] which adds an external velocity on the aerodynamics and structural rod components as well as on the inflow velocities of the thrusters.

The equations of motion of a rigid aircraft are given below. Due to the large attitude range, a unit quaternion \mathbf{q} [17] is used for attitude representation.

$$\begin{aligned}\dot{\mathbf{p}} &= \mathbf{R}(\mathbf{q}) \mathbf{v}_b \\ \dot{\mathbf{v}}_b &= \frac{1}{m} \mathbf{F}_b - \boldsymbol{\omega}_b \times \mathbf{v}_b \\ \dot{\mathbf{q}} &= \frac{1}{2} \mathbf{q} \otimes \begin{bmatrix} 0 \\ \boldsymbol{\omega}_b \end{bmatrix} \\ \dot{\boldsymbol{\omega}}_b &= \mathbf{I}^{-1} (\mathbf{M}_b - \boldsymbol{\omega}_b \times \mathbf{I} \boldsymbol{\omega}_b)\end{aligned}\quad (1)$$

where $\mathbf{R}(\mathbf{q})$ is the rotation matrix from body to inertial frame, which is retrieved from the unit quaternion \mathbf{q} , \mathbf{p} is the inertial position, $\mathbf{v}_b = [u, v, w]^T$ is the velocity in the body frame, m is the mass of the vehicle, $\boldsymbol{\omega}_b$ are the body angular rates in the body frame, \otimes is the quaternion product, \mathbf{I} is the inertia matrix of the vehicle, and \times is the 3D cross product. \mathbf{F}_b is the force acting at the CM of the vehicle, defined in the body frame, which is the sum the forces due to the gravity, the thrusters, the wing aerodynamics, the rods drag, and the contacts with the ground:

$$\mathbf{F}_b = \mathbf{F}_g + \mathbf{F}_t + \mathbf{F}_a + \mathbf{F}_r + \mathbf{F}_c \quad (2)$$

Similarly, $\mathbf{M}_b = [L, M, N]^T$ is the moment, in the body frame, acting at the CM of the vehicle, which is the sum of the moments due to the thrusters and gyroscopic effects, the aerodynamics, the rods drag, and the contacts with the ground:

$$\mathbf{M}_b = \mathbf{M}_t + \mathbf{M}_a + \mathbf{M}_r + \mathbf{M}_c \quad (3)$$

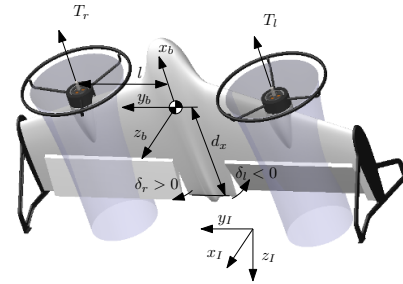


Fig. 1. Tailsitter CAD model showing the body and inertial frame, the four actuators, and the slipstream acting on a portion of the control surfaces. The deflections are defined positive along y_b using the right hand rule.

Gravity creates a force \mathbf{F}_g given by:

$$\mathbf{F}_g = \mathbf{R}(\mathbf{q})^T \begin{bmatrix} 0 \\ 0 \\ mg \end{bmatrix} \quad (4)$$

where g is the gravitational acceleration. The center of mass is located a distance d_x from the trailing edge and lies in the same plane as the thrusters' rotational axis and the chord line of the wings.

The inertia matrix \mathbf{I} was computed from a high fidelity CAD model, that includes hardware components. The mass from the CAD model matches at 92% the mass m of the aircraft measured on a scale.

A. Thrusters and Gyroscopic Moments

The thrusters produce a forward force \mathbf{F}_t , defined as:

$$\mathbf{F}_t = \begin{bmatrix} T_l + T_r \\ 0 \\ 0 \end{bmatrix} \quad (5)$$

Each thruster produces a torque Q about x_b axis and a yawing moment about z_b axis due to its lateral location at a distance l from the center of mass. Additionally, the gyroscopic moments are considered, which are proportional

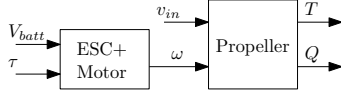


Fig. 2. Two-block representation of the thruster model.

to the body rates ω_b , the propellers' angular speeds ω_l and ω_r , and the thruster rotational inertia I_{th} about x_b axis:

$$\mathbf{M}_t = \begin{bmatrix} Q_r - Q_l \\ 0 \\ l(T_l - T_r) \end{bmatrix} + I_{th}(\omega_l - \omega_r) \begin{bmatrix} 0 \\ -\omega_{b,z} \\ \omega_{b,y} \end{bmatrix} \quad (6)$$

The thruster is modeled by two blocks, as shown in Fig. 2. The first block models the Electronic Speed Controller (ESC) and brushless motor, which generates the rotation ω of the propeller from the throttle τ and battery voltage V_{batt} . The second block is the propeller itself, which given its rotational speed ω and inflow velocity v_{in} , generates a thrust T and a torque Q . v_{in} is not the induced velocity, but the velocity at which the propeller move through the air.

The propeller angular speed ω is generated by the ESC and motor from the battery voltage V_{batt} and the throttle signal τ . It is modeled as an empirical function and will be discussed in section III-B:

$$\omega = \omega(V_{batt}, \tau) \quad (7)$$

Knowing the angular speed ω and the inflow velocity v_{in} , the propeller model is derived. First, the advance ratio J is computed. It represents the ratio of the inflow velocity over the propeller tip velocity. The notation from UIUC [18] is used:

$$J = \frac{\pi v_{in}}{\omega r_p} [1/rev] \quad (8)$$

where r_p is the radius of the propeller.

Then, the thrust coefficient C_T and power coefficient C_P are modeled as function of the advance ratio J . The model for these two coefficients will be described in section III-B.

$$C_T = C_T(J), \quad C_P = C_P(J) \quad (9)$$

Finally, the thrust force T and torque Q are computed as:

$$T = \frac{4}{\pi^2} \rho \omega^2 r_p^4 C_T, \quad Q = \frac{4}{\pi^3} \rho \omega^2 r_p^5 C_P \quad (10)$$

The model is the same for the left and right thruster. The torque Q is computed as a magnitude and equation 6 accounts for the direction.

B. Wing Aerodynamics and Rod Drag

The wing is modeled as a series of flat-plate segments. Each segment possesses its own velocity and surface and creates its own lift force, drag force, and pitching moment about its aerodynamic center. The forces and moments of each segment are then summed to form the aerodynamic force \mathbf{F}_a and aerodynamic moment \mathbf{M}_a . Although the airfoil section of the flying wing of the tailsitter is not a flat-plate, this model is chosen as formulas for aerodynamic forces and moments are available without need for experimental

tests. For this tailsitter, the flying wing is broken into nine horizontal segments and one vertical segment at each wingtip, refer to Fig. 3.

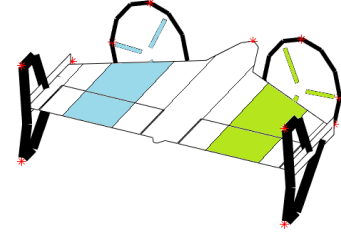


Fig. 3. Component breakdown. The blue components undergo the left slipstream, the green components undergo the right slipstream. The thick black components represent the structural components, modeled as rod segments creating drag forces. The corners for contact dynamics are represented by red stars (*).

The angle of attack α is the incidence angle formed between the incoming velocity and the chord line of the airfoil. It can be computed as $\alpha = \text{atan2}(w, u)$ when considering the whole aircraft or more generally, as $\alpha_i = \text{atan2}(w_i, u_i)$ when considering a segment i moving at a velocity $\mathbf{v}_i = [u_i, v_i, w_i]^T$. The velocity of any segment out of the slipstream is given by:

$$\mathbf{v}_i = \mathbf{v}_b + \omega_b \times \mathbf{r}_i - \mathbf{v}_w \quad (11)$$

where \mathbf{r}_i is the location of the i^{th} segment aerodynamic center in the body frame and \mathbf{v}_w is the wind velocity in the body frame computed from a Dryden wind model. This wind model generates 3D wind velocity components from white noise, then filters them with power spectral density transfer functions dependent on altitude [16]. For the segments inside a slipstream, only the longitudinal component u_i is modified since the thrusters blow along the longitudinal axis, respectively $u_i = v_{l,x}$ and $u_i = v_{r,x}$ for the segments behind the left and right thrusters. Momentum theory is used to predict the velocity downstream the propeller disc as [19]:

$$v_{l,x} = \sqrt{\frac{(u + rl)^2 + \frac{2T_l}{\rho\pi r_p^2}}{v_{in}}}, \quad v_{r,x} = \sqrt{\frac{(u - rl)^2 + \frac{2T_r}{\rho\pi r_p^2}}{v_{in}}} \quad (12)$$

where ρ is the usual air density in $[kg/m^3]$, and r_p is the propeller radius. The term v_{in} represents the forward velocity of the propeller moving through the air. In case of wind it becomes $v_{in} = (u \pm rl - v_{w,x})$. This is the same inflow velocity v_{in} as described in the thruster model in Fig 2. According to the same theory, when the airplane is static (i.e. $v_{in} = 0$), the diameter of the slipstream is given by $d_s = \sqrt{2}r_p$. This quantity is chosen for the width of the wing segments in the slipstream, shown as the green and blue segments on Figure 3. The elevons are not entirely in the slipstream.

Each horizontal segment i , having a mean aerodynamic chord c_i and span b_i , produces a force \mathbf{F}_i as:

$$\mathbf{F}_i = \frac{1}{2} \rho b_i c_i (u_i^2 + w_i^2) \begin{bmatrix} C_L \sin \alpha_i - C_D \cos \alpha_i \\ 0 \\ -C_L \cos \alpha_i - C_D \sin \alpha_i \end{bmatrix} \quad (13)$$

where C_L is the lift coefficient and C_D the drag coefficient, which are described further. Each horizontal segment, knowing their pitching moment at the aerodynamic center C_M , also produces a moment $\mathbf{M}_i = [0, M_i, 0]^T$:

$$M_i = \frac{1}{2} \rho b_i c_i^2 (u_i^2 + w_i^2) C_M \quad (14)$$

The segments aerodynamic forces and moments are then translated to the center of mass of the aircraft as:

$$\mathbf{F}_a = \sum \mathbf{F}_i, \quad \mathbf{M}_a = \sum (\mathbf{M}_i + \mathbf{r}_i \times \mathbf{F}_i) \quad (15)$$

In the linear range, the following lift curve slope is used for the flying wing segments, as described in [20]:

$$C_{L\alpha} = \frac{2\pi \cos \Lambda}{\frac{2 \cos \Lambda}{A_R} + \sqrt{1 + \left(\frac{2 \cos \Lambda}{A_R}\right)^2}} \quad (16)$$

where Λ is the sweep angle, and $A_R = b^2/S$ is the aspect ratio. Still in the linear range, the following equations are used to describe the lift and drag coefficients:

$$C_L = C_{L\alpha} \alpha, \quad C_D = C_{D,0} + \frac{C_L^2}{\pi k_0 A_R} \quad (17)$$

where $C_{D,0}$ is the drag coefficient due to skin friction, and k_0 is Oswald's efficiency factor.

As the angle of attack increases, the stalling phenomenon occurs progressively. To account for that, the model includes a term for progressive flow separation of the upper surface of the airfoil, starting from the trailing-edge, as well as turbulent leading edge vortices, which both cause a loss of lift. The angle of attack at complete stall α_{high} , which corresponds to a complete flow separation, is retrieved from an empirical database listing it for different flat plate aspect ratios. Regarding the control surface deflection, it has the effect of creating a camber on the wing segment and reducing the effective chord length, the consequences are a shift in the lift, drag, and moment curves and a modification of the stalling angle of attack α_{high} . For a complete set of equations, including stalling model, control surface deflection effects, vertical segments, sideslip effects, and moment coefficients, the reader can refer to [10]. The lift and drag coefficients of the entire aircraft are shown in Fig. 4 and the pitching moment coefficient of the entire aircraft is shown in Fig. 5.

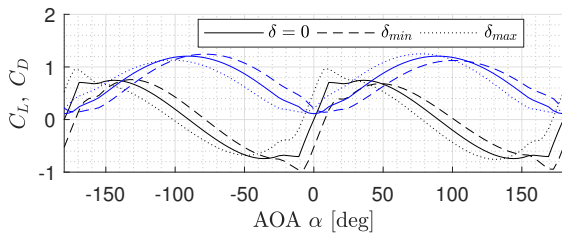


Fig. 4. Aerodynamic coefficients of the entire airplane. The lift coefficient C_L is shown in black and the drag coefficient C_D is shown in blue.

The structural parts such as the propeller protectors and the landing gear are modeled as rod segments creating a

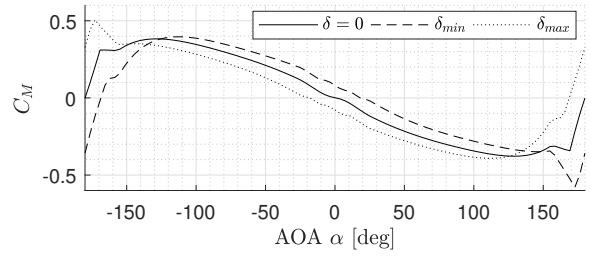


Fig. 5. Pitching moment coefficient C_M of the entire airplane.

drag force. Each rod segment j , of length l_j and diameter d_j , creates a drag force \mathbf{N}_j normal to its length, as shown in Fig. 6, with a magnitude [21] given by:

$$N_j = \frac{1}{2} \rho v_j^2 l_j d_j C_{D,rods} \sin^2 \theta_j \quad (18)$$

where the drag coefficient of the rods $C_{D,rods}$ is taken as 1.1. The rod segment velocity v_j can be computed using Eq. 11 by considering the center of the rod segment r_j as the location of the computed velocity. The rod segment forces are then translated to the center of mass as:

$$\mathbf{F}_r = \sum \mathbf{N}_j, \quad \mathbf{M}_r = \sum \mathbf{r}_j \times \mathbf{N}_j \quad (19)$$

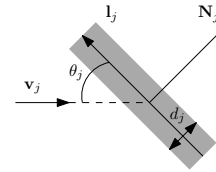


Fig. 6. Rod segment j in a wind field \mathbf{v}_j , with incidence angle θ_j , creating a normal force \mathbf{N}_j .

Each propeller protector is modeled as 12 rod segments composing the circle, plus 3 radial rods, all of them having a diameter of 3 [mm]. Each landing gear is composed of 6 rod segments, of diameter 7 [mm], as shown in Figure 3. According to this model, the rod drag force represents 40% of the total aerodynamic drag force when the aircraft is in level flight at 8 [m/s].

C. Ground Contact Dynamics

Since this study focuses on the full flight mission, including vertical takeoff and landing, there is a need to model ground contact dynamics. The contact force is modeled using a spring-damper analogy. In order to detect the contact with the ground, thirteen specific exterior points are selected, as shown by the red stars in Fig. 3.

Then, working in the inertial frame, each point k penetrating the ground at a depth d_k , and having a velocity $\mathbf{v}_{I,k}$, produces a force $\mathbf{F}_{I,k}$ at its respective location as:

$$\mathbf{F}_{I,k} = \begin{bmatrix} 0 \\ 0 \\ -m k_p d_k \end{bmatrix} - m k_v \mathbf{v}_{I,k} \quad (20)$$

The inertial velocity $\mathbf{v}_{I,k}$ is computed from the point's location in the body frame \mathbf{r}_k as:

$$\mathbf{v}_{I,k} = \mathbf{R}(\mathbf{q})(\mathbf{v}_b + \boldsymbol{\omega}_b \times \mathbf{r}_k) \quad (21)$$

To avoid unrealistic attraction to the ground, an upper bound of zero is imposed on the z_I component of the inertial force $\mathbf{F}_{I,k}$. These inertial forces are finally mapped into the body frame to generate the contact force \mathbf{F}_c and the contact moment \mathbf{M}_c :

$$\mathbf{F}_c = \sum \mathbf{R}(\mathbf{q})^T \mathbf{F}_{I,k}, \quad \mathbf{M}_c = \sum \mathbf{r}_k \times \mathbf{R}(\mathbf{q})^T \mathbf{F}_{I,k} \quad (22)$$

Satisfactory results are obtained for $k_p = 100 [1/s^2]$ and $k_v = 5 [1/s]$, i.e., the airplane landing phase was found to appear realistic during real time visualization and the airplane reaches a complete stop quickly, in about half a second.

D. Simplified Model

Distinct from the high fidelity simulator, a simplified analytic model describing the aircraft aerodynamics is needed for the controller developed in this research. This simplified model predicts the relation from the left and right throttle signals τ_l, τ_r and left and right elevon deflections δ_l, δ_r to the body moments $\mathbf{M}_b = [L, M, N]^T$ and the forward force F .

To distinguish variables evaluated in this model from those in the more exact model, we use an overhat notation to denote estimates. For example, \hat{M} denotes the pitching moment in the simplified model.

The forward force is estimated as the sum of the left and right thrust forces:

$$\hat{F} = T_l + T_r \quad (23)$$

where T_l and T_r are evaluated from τ_l and τ_r using the thruster model described in Figure 2.

The yawing moment is estimated from:

$$\hat{N} = l(T_l - T_r) \quad (24)$$

where l is the lateral position of the right thruster in the body frame.

The rolling moment \hat{L} is assumed to be the sum of the rolling moment generated by the elevons in the slipstream, the rolling moment generated by the elevons out of the slipstream, and the propeller torques:

$$\hat{L} = \frac{1}{2} \rho c_x (\delta_l v_l^2 - \delta_r v_r^2) + \frac{1}{2} \rho (u^2 + w^2) b_x (\delta_l - \delta_r) + (Q_r - Q_l) \quad (25)$$

where c_x is the rolling moment deflection coefficient accounting for the elevons in the slipstream, b_x is the rolling moment deflection coefficient accounting for the elevons outside the slipstream, Q_l and Q_r are the left and right propeller torques evaluated from the thruster model described in Figure 2, ρ is the air density, u and w are the aircraft velocity along x_B and z_B axes and v_l, v_r are the left and right slipstream velocities modeled using momentum theory:

$$v_l^2 = u^2 + w^2 + \frac{2T_l}{\rho \pi r_p^2}, \quad v_r^2 = u^2 + w^2 + \frac{2T_r}{\rho \pi r_p^2} \quad (26)$$

where r_p is the radius of the propeller.

Similarly, the pitching moment is assumed to be the sum of the pitching moment generated by the elevons in the slipstream, the pitching moment generated by the elevons outside the slipstream and the pitching moment at zero deflection.

$$\hat{M} = -\frac{1}{2} \rho c_y (\delta_l v_l^2 + \delta_r v_r^2) - \frac{1}{2} \rho (u^2 + w^2) b_y (\delta_l + \delta_r) + \hat{M}_0 \quad (27)$$

where c_y is the pitching moment deflection coefficient of the elevons in the slipstream, b_y is the pitching moment deflection coefficient of the elevons outside the slipstream. \hat{M}_0 is the estimated pitching moment of the entire aircraft at zero deflection, which is given by:

$$\hat{M}_0 = \frac{1}{2} \rho (u^2 + w^2) S \bar{c} \hat{C}_M(\alpha) \quad (28)$$

where S is the wing area, \bar{c} is the mean aerodynamic chord, and $\hat{C}_M(\alpha)$ is a 7th order polynomial function that fits the curve of the pitching moment coefficient at zero deflection, shown in Fig. 5.

The moment deflection coefficients c_x, c_y, b_x and b_y will be described in section III-A.

For compactness, the XZ dynamic pressure $P_d = \frac{1}{2} \rho (u^2 + w^2)$ as well as the left and right slipstream velocities defined in equation 26 can be used in equations 25 and 27. We finally obtain the following set of equations describing the simplified analytical aerodynamic model:

$$\begin{aligned} \hat{L} &= \frac{c_x}{\pi r_p^2} (\delta_l T_l - \delta_r T_r) + P_d b_x (\delta_l - \delta_r) + (Q_r - Q_l) \\ \hat{M} &= -\frac{c_y}{\pi r_p^2} (\delta_l T_l + \delta_r T_r) - P_d (c_y + b_y) (\delta_l + \delta_r) + \hat{M}_0 \\ \hat{N} &= l(T_l - T_r) \\ \hat{F} &= T_l + T_r \end{aligned} \quad (29)$$

III. COEFFICIENT EVALUATION

In addition to the theoretical data, two static bench tests were conducted using a force torque sensor. The first set of tests aimed to evaluate the control surfaces effectiveness, and the second set of tests allowed us to create a representative model for the thrusters.

A. Control Surface Coefficients

Ideally, the lift and drag forces should be measured to validate the flat plate model for this specific aircraft. While no wind tunnel was used at this stage, the effects of the left and right control surface deflections δ_l and δ_r , as functions of the slipstream velocity, were investigated. The whole airplane was mounted on the force torque sensor to measure the elevon deflection coefficients c_x and c_y used to predict the moments linearly. From the rolling moment \hat{L} and pitching moment \hat{M} in Eq. 29, considering the airplane fixed during this bench test ($P_d = 0, \hat{M}_0 = 0$) and both thrust forces set

equal and constant ($T_l = T_r = T$, $Q_l = Q_r$), the following relations are obtained:

$$\begin{aligned}\hat{L} &= \frac{c_x}{\pi r_p^2} T(\delta_l - \delta_r) \\ \hat{M} &= -\frac{c_y}{\pi r_p^2} T(\delta_l + \delta_r)\end{aligned}\quad (30)$$

Exploiting the symmetry in these relations, first c_x can be obtained from the rolling moment L measured by the torque sensor, by applying symmetrically opposite deflections to the left and right elevons $\delta_l = -\delta_r = \delta$:

$$c_x = \frac{L \pi r_p^2}{2T \delta} \quad (31)$$

and then c_y can be obtained from the pitching moment M measured by the torque sensor, by applying symmetric deflections to the elevons $\delta_l = \delta_r = \delta$:

$$c_y = -\frac{M \pi r_p^2}{2T \delta} \quad (32)$$

The coefficients are taken as the mean of several measurements, and the resulting values are:

$$c_x = 9.91 \cdot 10^{-4} [m^3/rad], \quad c_y = 4.74 \cdot 10^{-4} [m^3/rad] \quad (33)$$

A similar procedure was conducted in the simulator to retrieve the coefficients in order to compare them:

$$c_{x,sim} = 2.35 \cdot 10^{-3} [m^3/rad], \quad c_{y,sim} = 3.5 \cdot 10^{-4} [m^3/rad] \quad (34)$$

An analogous procedure was used to obtain a value for the coefficients out of the slipstream, namely b_x and b_y , given the airplane flying at a constant velocity in the simulated environment.

The value of c_x and from the simulator is about 2.5 times the measured value, while the value of c_y is about 25% lower in the simulator, indicating that the control surfaces are more effective than predicted for the pitching moment and much less effective than predicted for the rolling moment. The same trend was observed when flying the real platform manually and flying the aircraft manually in the simulated environment. In real flight, vertical loop maneuvers were found to be quicker and roll maneuvers were observed to be much slower than when performing the same maneuvers in the simulator. This large disparity between the measured and simulated values is likely due to assumptions in the model, such as the fact that momentum theory was used to predict the slipstream over the elevons and the fact that a flat plate model was used. The measured values are considered more representative of the real aerodynamics than the simulated coefficient values.

In order to make use of the experimental measurements to improve the simulator, we chose to scale the rolling moment due to deflection by $c_x/c_{x,sim}$ and the pitching moment due to deflection by $c_y/c_{y,sim}$. For this purpose, the rolling and pitching moments at the given elevon deflection and the rolling and pitching moments at zero deflection are computed

and the moments predicted by the simulator are set to:

$$\begin{aligned}L &= L(\delta = 0) + \frac{c_x}{c_{x,sim}} (L(\delta_l, \delta_r) - L(\delta = 0)) \\ M &= M(\delta = 0) + \frac{c_y}{c_{y,sim}} (M(\delta_l, \delta_r) - M(\delta = 0))\end{aligned}\quad (35)$$

B. Thruster Coefficients

In this section, the coefficients used in the thruster model given in section II-A are retrieved from experiments. First, a model is proposed for the ESC and motor block relating the angular speed of the propeller given the battery voltage and throttle signal. Then the thrust and power coefficients are investigated.

To measure the ESC and motor properties, the whole thruster, with the propeller was fixed on a static surface. A DC power source was used to provide voltage to the ESC. The throttle signals were converted to PWM signals and sent to the ESC. The angular speed of the propeller was obtained from an oscilloscope measuring the differential frequency between two phases of the brushless motor and this measure was validated by an optical RPM sensor.

The propeller angular speed was measured for different voltages and throttle signals, providing the data points shown in 7. To better understand the effect of the battery voltage, the data points at each voltage were scaled as functions of that voltage. It was found that, when they were scaled by $V_{batt}^{0.8}$ the data at different voltages collapsed approximately onto a single line. That line was then curve-fitted using a second-order polynomial, leading to the following model:

$$\omega_p = V_{batt}^{0.8} \left(\underbrace{-84.75}_{\omega_{p,2}} \tau^2 + \underbrace{356.34}_{\omega_{p,1}} \tau - \underbrace{4.27}_{\omega_{p,0}} \right) \quad (36)$$

This model with the recorded data are shown in Figure 7. Equation 36 was used to fill the role of equation 7 described earlier.

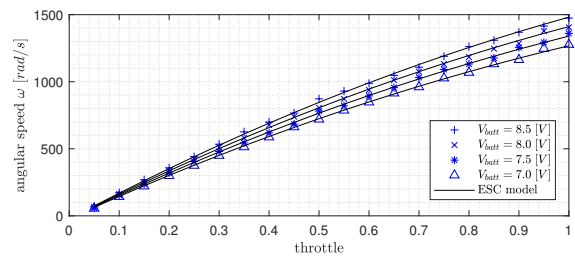


Fig. 7. Propeller angular speed ω as a function of throttle at different battery voltages V_{batt} .

To evaluate the thrust coefficient C_T and power coefficient C_P , a wind tunnel experiment is needed to estimate them as function of the inflow velocity v_{in} , or equivalently as a function of the advance ratio J . Rather than conduct our own wind tunnel experiments, we first performed experiments at zero inflow velocity ($J = 0$) and relied on a public database to complete the model for nonzero J .

The thruster was mounted on a force torque sensor. The propeller thrust T and torque Q were recorded at different

propeller angular speeds ω_p . Then, the static thrust and power coefficients were obtained using:

$$C_{T,0} = \frac{T \pi^2}{4 \rho \omega^2 r_p^4}, \quad C_{P,0} = \frac{Q \pi^3}{4 \rho \omega^2 r_p^5} \quad (37)$$

where ρ is the ambient air density and r_p the radius of the propeller.

Then, a propeller with similar static characteristics (GWS Direct Drive 4.5x3 inches) was chosen from the UIUC database [18] and its thrust and power coefficients were curve fitted and scaled to match the mean static coefficients of the propeller in this experiment. The thrust and power coefficients are shown in Fig. 8 and their values are obtained as:

$$\begin{aligned} C_T(J) &= -0.1281J^2 - 0.1196J + 0.1342 \\ C_P(J) &= -0.0602J^2 - 0.0146J + 0.0522 \end{aligned} \quad (38)$$

For negative advance ratios, which occur during vertical descent, the static coefficients are used. For small negative advance ratios ($-0.3 < J < 0$), this assumption is validated by experimental data [22].

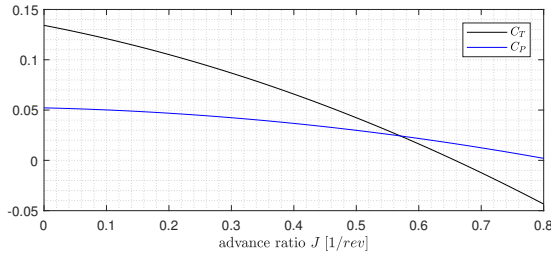


Fig. 8. Thrust and power coefficients as functions of advance ratio.

IV. CONTROLLER

A quaternion-based controller from [15] is implemented in the current platform, and works as follows. First, a maneuver generator generates the reference position \mathbf{p}_{ref} , the reference attitude \mathbf{q}_{ref} and the reference longitudinal velocity u_{ref} . Then, using the current position and attitude \mathbf{p} and \mathbf{q} , the position controller will modify the reference attitude \mathbf{q}_{ref} into the desired attitude \mathbf{q}_{des} to orient the thrust force towards the reference position. At the same time, the thrust controller generates a desired forward force F_d to track the altitude $h_{ref} = -p_{ref,z}$ and the longitudinal velocity u_{ref} . The attitude controller generates the desired moments $\mathbf{M}_d = [L_d, M_d, N_d]^T$ by computing the quaternion attitude error from the actual attitude \mathbf{q} and the desired attitude \mathbf{q}_{des} . A PD law is then applied on this quaternion

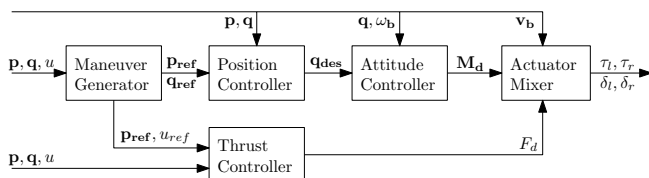


Fig. 9. Block diagram of the cascaded quaternion controller.

error. Finally the mixer, using the simplified aerodynamic model from Section II-D, generates the desired left and right throttle and deflection signals $\tau_l, \tau_r, \delta_l, \delta_r$ respectively, to achieve these desired moments and forward force. This design, being developed for aerobatic maneuvers, allows the same controller to be used for all the flight phases.

A. Maneuver Generator

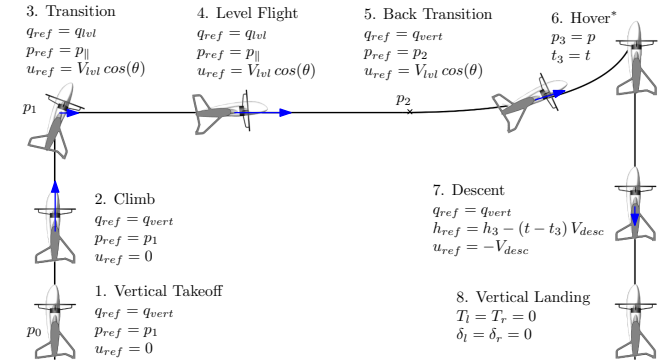


Fig. 10. Maneuver generator final state machine for a minimal VTOL flight mission.

The maneuver generator is implemented as a finite state machine to ensure a consistent logic. It generates the reference position \mathbf{p}_{ref} , attitude \mathbf{q}_{ref} and longitudinal velocity u_{ref} at each instant to perform the minimal flight mission shown in Fig. 10. First, it sets the reference position as \mathbf{p}_1 as well as the reference attitude as the vertical attitude \mathbf{q}_v . The position \mathbf{p}_1 is the position at level altitude above the starting point. The vertical attitude is retrieved from Euler angles and the initial heading ψ_0 as:

$$\mathbf{q}_v = \mathbf{q}(\phi = 0, \theta = \pi/2, \psi = \psi_0) \quad (39)$$

Then, just before reaching the level altitude, the transition occurs. The reference position becomes $\mathbf{p}_{||}$: the current position, projected to a line created at the level altitude with the initial heading. The reference attitude becomes the level flight attitude :

$$\mathbf{q}_{lvl} = \mathbf{q}(\phi = 0, \theta_{lvl}, \psi = \psi_0) \quad (40)$$

where θ_{lvl} is the pre-computed equilibrium pitch angle accounting for the wing lift, as a function of the level flight velocity, as proposed in [15]. Because the level flight is in the linear region of the lift curve slope, Eq. 17 is used to compute it. According to the simulator, the maximum achievable level flight velocity for this platform is 15 [m/s]—limited when the drag forces which become greater than the maximum thrust.

After \mathbf{p}_2 being reached, the back transition occurs. The reference attitude is set to \mathbf{q}_v and the reference position is set to \mathbf{p}_2 , intentionally behind the airplane, to ensure a short back transition. Looking at the pitching moment coefficient in Fig. 5, for this particular tailsitter, the moment produced by the elevons in forward flight is not able to counteract the natural pitching moment M_0 beyond an angle of attack $\alpha = 17$ [deg],

i.e. the overall pitching moment is not zero. This means that it is not possible to achieve the back transition from level to hover by maintaining constant altitude and increasing the pitch angle, which in this case equals the angle of attack. In fact, the minimum achievable velocity in level flight is 7 [m/s], below that limit, a bigger angle of attack would be needed. It is however possible to achieve the back transition by gaining altitude and describing a portion of a circle as depicted in Figure 10.

When the aircraft's attitude starts to point backward (i.e. $|\psi - \psi_0| > 90^\circ$), the hover to descent state takes place and the current position and time are saved, but this is not a holding state. Finally the descent occurs in backward flight, the aircraft tracks the descent velocity $u_{ref} = -V_{desc}$ and the reference position is decreased in altitude with time. The flight mission is terminated by stopping the actuators when the altitude is close to the ground, in order to land. This abrupt landing method is used to prevent ground contact forces to interfere with the controller.

B. Thrust Controller

The objective of the thrust controller is to generate the forward force F_d to track the reference altitude $h_{ref} = -p_{ref,z}$ and reference longitudinal velocity u_{ref} . The control law is defined as follows:

$$F_d = \max \left(0, mg \sin \theta + m k_{up}(u_{ref} - u) + m k_{hp}(h_{ref} - h) \sin \theta \right) \quad (41)$$

where θ is the pitch angle, and the max function ensures a positive longitudinal force. The aerodynamic lift and drag forces are not accounted for in the thrust controller as they are highly nonlinear and have little effect on the altitude and longitudinal velocity tracking.

C. Position Controller

From the reference attitude \mathbf{q}_{ref} , the position controller generates the desired attitude \mathbf{q}_{des} to reorient the thrust force towards the reference position \mathbf{p}_{ref} . It generates the correction angles Θ_y and Θ_z , from the position error, by computing a PD control law, using the positive gains k_{pp} and k_{pd} respectively:

$$\begin{bmatrix} - \\ \Theta_z \\ \Theta_y \end{bmatrix} = \mathbf{R}_r \left(k_{pp} (\mathbf{p}_{ref} - \mathbf{p}) + k_{pd} \frac{d}{dt} (\mathbf{p}_{ref} - \mathbf{p}) \right) \quad (42)$$

where $\mathbf{R}_r = \mathbf{R}(\mathbf{q}_{ref})$ is the rotation matrix from the inertial to the reference attitude and can be found from the reference quaternion \mathbf{q}_{ref} . The correction angles Θ_y and Θ_z are bounded to $\pm 15^\circ$ for stability reasons during hover. To account for lateral correction by banking the aircraft, Θ_x is introduced as:

$$\Theta_x = \Theta_z \cos \theta \cos \phi \quad (43)$$

Then, the correction angles are translated into unit quaternions as follows:

$$\begin{aligned} \mathbf{q}_x &= [\cos \frac{\Theta_x}{2}, \sin \frac{\Theta_x}{2}, 0, 0] \\ \mathbf{q}_y &= [\cos \frac{\Theta_y}{2}, 0, -\sin \frac{\Theta_y}{2}, 0] \\ \mathbf{q}_z &= [\cos \frac{\Theta_z}{2}, 0, 0, \sin \frac{\Theta_z}{2}] \end{aligned} \quad (44)$$

Finally the desired attitude \mathbf{q}_{des} is computed by rotating the reference attitude obtained from the maneuver generator \mathbf{q}_{ref} around z axis (yaw), then around y axis (pitch) and finally around x axis (roll):

$$\mathbf{q}_{des} = \mathbf{q}_{ref} \otimes \mathbf{q}_z \otimes \mathbf{q}_y \otimes \mathbf{q}_x \quad (45)$$

D. Attitude Controller

The attitude controller generates the desired moments L_d, M_d, N_d from the attitude error $\Delta \mathbf{q}$. The attitude error can be obtained by multiplying the conjugated attitude \mathbf{q}^* by the desired attitude \mathbf{q}_{des} or its negation (which describes the same attitude):

$$\Delta \mathbf{q} = \begin{cases} \mathbf{q}^* \otimes \mathbf{q}_{des}, & \text{if } \|\mathbf{q} - \mathbf{q}_{des}\| \leq \|\mathbf{q} + \mathbf{q}_{des}\| \\ \mathbf{q}^* \otimes (-\mathbf{q}_{des}), & \text{if } \|\mathbf{q} - \mathbf{q}_{des}\| > \|\mathbf{q} + \mathbf{q}_{des}\| \end{cases} \quad (46)$$

where the case ensures the angular errors remain less than 180° .

The desired moments $\mathbf{M}_d = [L_d, M_d, N_d]^T$ are then computed by multiplying the inertia with a PD control law on the vector part of the quaternion $\Delta \mathbf{q}_{1:3}$ and the body rates ω_b :

$$\mathbf{M}_d = \mathbf{I} (k_{ap} \Delta \mathbf{q}_{1:3} + k_{ad} \omega_b) \quad (47)$$

where k_{ap} and k_{ad} are the positive PD gains.

E. Actuator Allocation

The last module of the controller is the actuator mixer. Its goal is to translate the desired forward force F_d and desired moments $\mathbf{M}_d = [L_d, M_d, N_d]^T$ into actuator signals, namely the left and right throttle signals τ_l, τ_r and the left and right elevons deflections δ_l, δ_r . For this purpose, the simplified model from Eq. 29 is inverted and the desired moments and forward force are assumed be described by it (i.e. $\mathbf{M}_d = [\hat{L}, \hat{M}, \hat{N}]^T$ and $F_d = \hat{F}$).

First, a upper bound of 95% of the maximum longitudinal force at the current flying conditions is set on F_d . This is used to keep room for yawing authority achieved by differential thrust. The maximum thrust force of one thruster T_{max} can be retrieved using the forward thruster model in Section II-A and feeding it the current battery voltage, forward velocity and maximum throttle signal. This upper bound F_{max} is then set as:

$$F_{max} = 2 \cdot 0.95 \cdot T_{max} \quad (48)$$

The actuator mixer then solves the left and right thrust forces from F_d and N_d :

$$T_l = \frac{1}{2} F_d + \frac{1}{2l} N_d, \quad T_r = \frac{1}{2} F_d - \frac{1}{2l} N_d \quad (49)$$

where l is the lateral distance from the center of mass to the right thruster. Then, a lower bound T_{min} is set on the thrust forces to keep a minimum slipstream velocity $v_{s,min}$ over the elevons and ensure control surface effectiveness:

$$T_{min} = \frac{1}{2} \rho \pi r_p^2 (v_{s,min}^2 - u^2) \quad (50)$$

At this point, the left and right torques Q_l, Q_r and the left and right throttles τ_l, τ_r , can be computed from the left and right thrust forces T_l, T_r , knowing the longitudinal velocity u . The propeller model from section II-A can easily be inverted since all the sub models are second order polynomials. Knowing T_l, T_r, Q_l, Q_r, L_d and M_d , the left and right deflections can be solved as the following linear system:

$$A \begin{bmatrix} \delta_l \\ \delta_r \end{bmatrix} = \underbrace{\begin{bmatrix} L_d - (Q_r - Q_l) \\ M_d - M_0 \end{bmatrix}}_b \Rightarrow \begin{bmatrix} \delta_l \\ \delta_r \end{bmatrix} = A^{-1} b \quad (51)$$

$$A = \begin{bmatrix} \frac{c_x}{\pi r_p^2} T_l + P_d b_x & -\frac{c_x}{\pi r_p^2} T_r - P_d b_x \\ -\frac{c_y}{\pi r_p^2} T_l - P_d (c_y + b_y) & -\frac{c_y}{\pi r_p^2} T_r - P_d (c_y + b_y) \end{bmatrix} \quad (52)$$

A is invertible as long as there is a nonzero velocity on the control surfaces, which is the case due to $v_{s,min}$.

If the pitching moment is too weak, and the mean elevon deflection $\bar{\delta} = \frac{1}{2}(\delta_l + \delta_r)$ is not zero, the pitching moment can be boosted by increasing the slipstream velocities by modifying the desired longitudinal force as:

$$F_d = \frac{M_d - \hat{M}_0 + 2P_d(c_y + b_y)\bar{\delta}}{-\frac{c_y}{\pi r_p^2}\bar{\delta}} \quad (53)$$

the mixer is then recomputed from Eq. 48 to Eq. 52.

V. SIMULATION RESULTS

A minimal VTOL flight mission is executed in the real-time simulator using the finite state maneuver generator. The flight mission is set as follows. The airplane starts vertically facing the North direction, takes off vertically and climbs to an altitude of 5 [m]. Then transitions to level flight pointing North, tracks an altitude of 6 [m] and a ground velocity of 7 [m/s]. At this velocity, the reference pitch angle is given as $\theta_{lvl} = 14.3^\circ$. After travelling 40 [m] horizontally, the back transition occurs. The vehicle descends in backward flight at a velocity of 0.5 [m/s] and lands when it is 5 [cm] above the ground.

In this simulation environment, the controller is fed back perfect states (i.e. no sensor noise is included), but a North East wind with mean velocity of 1 [m/s] is present for realism. The aircraft parameters are shown in Appendix Table I and the controller gains are shown in Appendix Table II.

The simulation results are shown in Fig.11 and 12. The first expected observation is the discontinuity of the reference signals sent to the controller, such as the altitude h_{ref} or the position x_{ref} . In spite of these discontinuities, the controller is able to maintain stability during all flight modes.

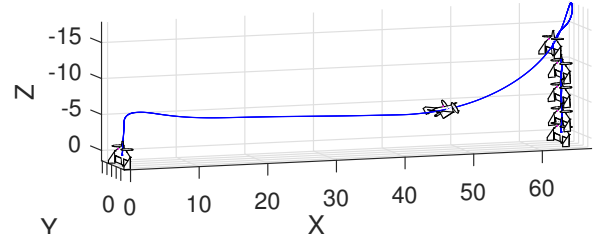


Fig. 11. Trajectory of the VTOL flight mission. The airplane is not to scale.

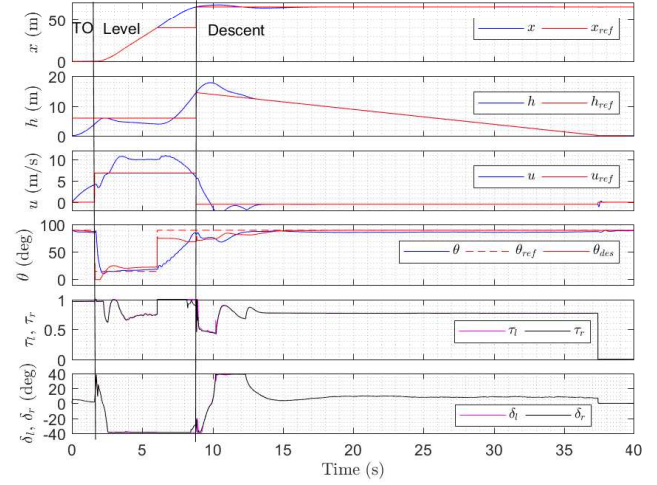


Fig. 12. Simulation results time history. Top to bottom: North position x and reference x_{ref} , altitude h and reference h_{ref} , longitudinal velocity u and reference u_{ref} , pitch angle θ , reference θ_{ref} and desired θ_{des} , left and right propeller rotational speeds ω_l, ω_r , left and right elevon deflection δ_l, δ_r .

The climb phase lasts less than 2 [s] while the thrusters are saturated at 95%. The level flight lasts about 4 [s] and covers a distance of 40 [m], good altitude tracking is observed with an error less than 2 [m]. The speed u is about 3.5 [m/s] faster than its reference u_{ref} during the level flight, and the elevons are observed to be saturated, which means the platform is overweight. The thrust controller is in a tradeoff of increasing the thrust to reduce altitude error and reduce the thrust to reduce velocity error. The lateral position error is likely due to the North East wind and the maximum error of about 5 [m] occurs at the end of the back transition. Good tracking is observed during the descent phase, nonetheless this phase is the longest due to the difficulty of backward flight.

Of particular interest is the back transition, the airplane needs to climb about 12 meters to complete it, as explained in section IV-A, and takes about 27 [m] horizontally. Due to the saturation of all the actuators, it is likely the minimum stopping distance for this platform.

VI. CONCLUSION

The work presented in this research includes a high fidelity simulator along with a single controller to control all flight regimes encountered by a tailsitter vehicle. The simulator

captures detailed aerodynamics such as progressive stall, the effect of large control deflections, and structural component drag. Thruster dynamics along with slipstream effects are also modeled as well as a simple yet effective ground contact model. The controller uses a cascaded design that allows reusability. Other than a few modifications, only the actuator mixer was redesigned. Successful results were observed in simulation demonstrating its suitability for this aircraft as well as the simulator's abilities to reproduce the complex behavior of a tailsitter vehicle.

Future work will include a hardware-in-the-loop (HIL) simulation, where the controller is running on the real hardware while connected to the simulator. The HIL will be used to validate the behavior of the controller observed in pure simulations, in a more realistic environment which includes the real state estimator and realistic sensor noise. Real flight experiments will be performed to demonstrate the autonomous ability of this system as well as evaluate the performance of the developed simulator. Future development could also include validation of the aerodynamics in a wind tunnel and extension of the maneuver generator to track any trajectory given as a sequence of positions.

APPENDIX

TABLE I
AIRCRAFT PROPERTIES

Parameter	Symbol	Value	Units
Mass	m	0.21	kg
Moment of Inertia	I_x	$3.0 \cdot 10^{-3}$	$kg m^2$
	I_y	$6.2 \cdot 10^{-4}$	$kg m^2$
	I_z	$3.5 \cdot 10^{-3}$	$kg m^2$
Non-zero Products of Inertia	I_{xz}	$-14 \cdot 10^{-6}$	$kg m^2$
Wing Area	S	0.08	m^2
Mean Aerodynamic Chord	\bar{c}	0.17	m
Wing Span	b	0.5	m
Control Derivative Coefficients	c_x	$9.91 \cdot 10^{-4}$	m^3/rad
	c_y	$4.74 \cdot 10^{-4}$	m^3/rad
	b_x	$9.37 \cdot 10^{-4}$	m^3/rad
	b_y	$3.48 \cdot 10^{-4}$	m^3/rad
Maximum Elevons Deflection	δ_{max}	39	deg
Propeller Radius	r_p	62.5	mm
Thruster Rotational Inertia	I_{th}	$1.6 \cdot 10^{-6}$	$kg m^2$
Thrusters Lateral Position	l	145	mm
CM Position from Trailing Edge	d_x	130	mm
Delta Wing Sweep Angle	Λ	19.8	deg
Battery Voltage	V_{batt}	7.4	V
Skin Friction Coefficient	$C_{D,0}$	0.02	
Oswald's Efficiency Factor	k_0	0.87	

TABLE II
CONTROLLER GAINS

Parameter	Symbol	Value	Units
Position Proportional Gain	k_{pp}	0.06	rad/m
Position Derivative Gain	k_{pd}	0.1	rad s/m
Attitude Proportional Gain	k_{ap}	700	1/s ²
Attitude Derivative Gain	k_{ad}	60	1/s
Speed Proportional Gain	k_{up}	8	1/s
Height Proportional Gain	k_{hp}	18	1/s ²
Minimum Slipstream Velocity	$v_{s,min}$	8	m/s

REFERENCES

- [1] N. Muchiri and S. Kimathi, "A review of applications and potential applications of uav," in *Proceedings of Sustainable Research and Innovation Conference*, pp. 280–283, 2016.
- [2] A. S. Saeed, A. B. Younes, S. Islam, J. Dias, L. Seneviratne, and G. Cai, "A review on the platform design, dynamic modeling and control of hybrid uavs," in *Unmanned Aircraft Systems (ICUAS), 2015 International Conference on*, pp. 806–815, IEEE, 2015.
- [3] L. R. Lustosa, F. Defay, and J.-M. Moschetta, "Longitudinal study of a tilt-body vehicle: modeling, control and stability analysis," in *Unmanned Aircraft Systems (ICUAS), 2015 International Conference on*, pp. 816–824, IEEE, 2015.
- [4] R. Ritz and R. D'Andrea, "A global controller for flying wing tailsitter vehicles," in *Robotics and Automation (ICRA), 2017 IEEE International Conference on*, pp. 2731–2738, IEEE, 2017.
- [5] R. F. Stengel, *Flight dynamics*. Princeton University Press, 2015.
- [6] R. W. Beard and T. W. McLain, *Small unmanned aircraft: Theory and practice*. Princeton university press, 2012.
- [7] W. Khan, *Dynamics modeling of agile fixed-wing unmanned aerial vehicles*. Phd thesis, McGill University, 2016.
- [8] S. Verling, B. Weibel, M. Boosfeld, K. Alexis, M. Burri, and R. Siegwart, "Full attitude control of a vtol tailsitter uav," in *Robotics and Automation (ICRA), 2016 IEEE International Conference on*, pp. 3006–3012, IEEE, 2016.
- [9] M. S. Selig, "Real-time flight simulation of highly maneuverable unmanned aerial vehicles," *Journal of Aircraft*, 2014.
- [10] W. Khan and M. Nahon, "Modeling dynamics of agile fixed-wing uavs for real-time applications," in *Unmanned Aircraft Systems (ICUAS), 2016 International Conference on*, pp. 1303–1312, IEEE, 2016.
- [11] V. Myrand-Lapierre, A. Desbiens, E. Gagnon, F. Wong, and É. Poulin, "Transitions between level flight and hovering for a fixed-wing mini aerial vehicle," in *American Control Conference (ACC), 2010*, pp. 530–535, IEEE, 2010.
- [12] Y. Jung and D. H. Shim, "Development and application of controller for transition flight of tail-sitter uav," *Journal of Intelligent & Robotic Systems*, vol. 65, no. 1, pp. 137–152, 2012.
- [13] P. Casau, D. Cabecinhas, and C. Silvestre, "Hybrid control strategy for the autonomous transition flight of a fixed-wing aircraft," *IEEE Transactions on control systems technology*, vol. 21, no. 6, pp. 2194–2211, 2013.
- [14] N. B. Knoebel and T. W. McLain, "Adaptive quaternion control of a miniature tailsitter uav," in *American Control Conference, 2008*, pp. 2340–2345, IEEE, 2008.
- [15] E. Bulka and M. Nahon, "Autonomous control of agile fixed-wing uavs performing aerobatic maneuvers," in *Unmanned Aircraft Systems (ICUAS), 2017 International Conference on*, pp. 104–113, IEEE, 2017.
- [16] K. Wilhelm, "Military standard-flying qualities of piloted aircraft," tech. rep., MIL-STD-1797, US Air Force Department, 1990.
- [17] A. L'Afflito, *A Mathematical Perspective on Flight Dynamics and Control*. Springer, 2017.
- [18] J.B. Brandt, R.W. Deters, G.K. Ananda, and M.S. Selig, "UIUC Propeller Database." <http://m-selig.ae.illinois.edu/props/propDB.html>, 2005-2015.
- [19] B. W. McCormick, *Aerodynamics, aeronautics, and flight mechanics*, vol. 2. Wiley New York, 1995.
- [20] J. D. Anderson Jr, *Fundamentals of aerodynamics*. Tata McGraw-Hill Education, 2010.
- [21] S. F. Hoerner, *Fluid-dynamic drag: practical information on aerodynamic drag and hydrodynamic resistance*. Hoerner Fluid Dynamics, 1965.
- [22] O. Shetty and M. Selig, "Small-scale propellers operating in the vortex ring state," in *49th AIAA Aerospace Sciences Meeting including the New Horizons Forum and Aerospace Exposition*, p. 1254, 2011.